

# 1 **Multiscale modeling of ion diffusion in cement paste:** 2 **electrical double layer effects**

3 **Yuankai Yang<sup>(1)</sup>, Ravi A. Patel<sup>(2)</sup>, Sergey V. Churakov<sup>(2,3),‡</sup>, Nikolaos I.**  
4 **Prasianakis<sup>(2)</sup>, Georg Kosakowski<sup>(2)</sup> and Moran Wang<sup>(1),†</sup>**

5 (1) Department of Engineering Mechanics and CNMM, Tsinghua University, Beijing 100084, China

6 (2) Laboratory for Waste Management, Paul Scherrer Institute, Villigen 5232, Switzerland

7 (3) Institute of Geological Sciences, University of Bern, Bern 3012, Switzerland

## 8 **Abstract**

9 Understanding the mechanism of ion diffusion in hardened cement paste is of great  
10 importance for predicting long-term durability of concrete structures. Gel pores in  
11 calcium silicate hydrate (C-S-H) phase forms dominant pathway for transport in cement  
12 paste with low w/c ratios where the electrical double layer effects play an important  
13 role. Experimental results suggest that the effective diffusivity of chloride ions is  
14 similar as that of tritiated water (HTO) and higher than the sodium ions. This difference  
15 can be attributed to the electrical double layer near the charged C-S-H surfaces. In order  
16 to understand species transport processes in C-S-H and to quantify its effective  
17 diffusivity, a multiscale modelling technique has been proposed to combine atomic-  
18 scale and pore-scale modeling. At the pore-scale, the lattice Boltzmann method is used  
19 to solve a modified Nernst Planck equation to model transport of ions in gel pores. The  
20 modified Nernst Planck equation accounts for steric and ion-ion correlation effects by  
21 using correction term for excess chemical potential computed using the results from the  
22 grand canonical Monte Carlo scheme at atomic scale and in turn bridges atomic scale  
23 model with pore scale model. Quantitative analysis of pore size influence on effective  
24 diffusivity carried out by this multiscale model shows that the contribution of the Stern  
25 layer to ion transport is not negligible for pores with diameter less than 10 nm. The  
26 developed model is able to reproduce qualitatively the trends of the diffusivity of  
27 different ions reported in literature.

28

29 **Keywords:** multiscale modeling; effective diffusivity; electrical double layer; C-S-H

---

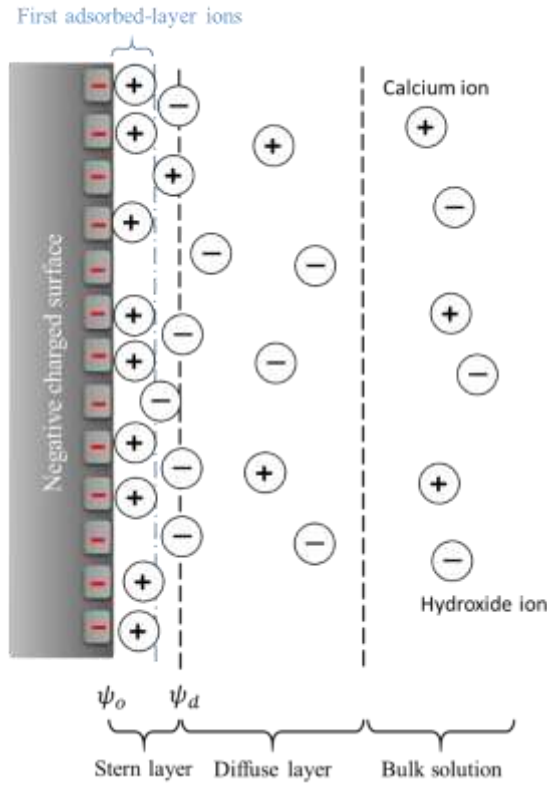
† Corresponding author, Email: [mrwang@tsinghua.edu.cn](mailto:mrwang@tsinghua.edu.cn)

‡ Corresponding author, Email: [sergey.churakov@psi.ch](mailto:sergey.churakov@psi.ch)

## 30 **1. Introduction**

31 The ability of ion to transport through cementitious materials influences the extent of  
32 several degradation mechanisms such as sulphate attack, carbonation, leaching,  
33 chloride transport in marine structures and contaminant transport in hazardous waste  
34 disposal systems. Therefore, improving the understanding of the ion transport  
35 mechanisms through cementitious materials is of great importance for predicting the  
36 long-term performance and service life of concrete structures. In the absence of pressure  
37 gradient (advection), diffusion is the key transport ion mechanism in cementitious  
38 materials which can be characterized by the effective diffusivity of the media. The pore  
39 space for ion diffusion in cement paste can be distinguished (in absence of defects such  
40 as micro-cracks) into capillary pores, submicron capillary and gel pores in calcium  
41 silicate hydrate (C-S-H) phase. The dominant pore space can be distinguished using the  
42 concept of capillary pore percolation [1]. When the capillary porosity depercolates, the  
43 gel pores in calcium silicate hydrate (C-S-H) phase forms the dominant pathway for  
44 transport in cement paste [2]. At this stage nano-scale effects on ion transport would  
45 play important role.

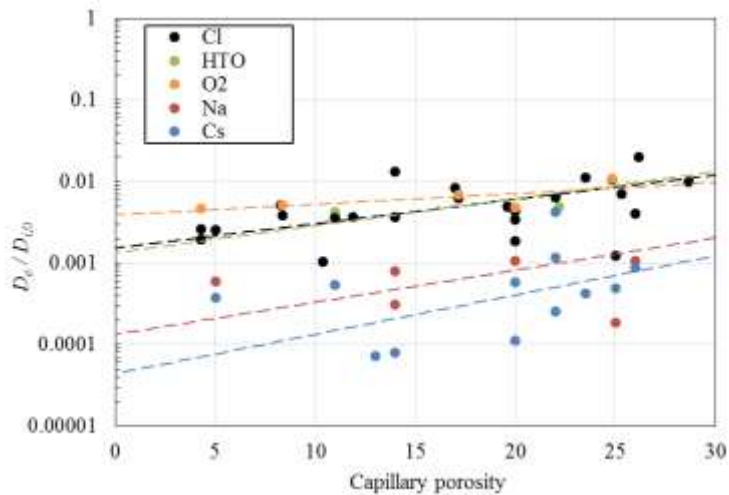
46



47

48 Fig. 1 A sketch of the structure of electrical double layer near the charged C-S-H surface. The pore  
 49 solution is  $\text{Ca}(\text{OH})_2$ . In the high- $p\text{H}$  pore solution, the C-S-H surface is usually negative charged, but the  
 50 bivalent calcium ions can over balance the negative charge on the surface, which cause the positive zeta  
 51 potential  $\psi_d$ . This phenomenon is named as charge reversal [3].

52



53

54 Fig. 2 The relative effective diffusion coefficients of  $\text{Na}^+$ ,  $\text{Cl}^-$ ,  $\text{Cs}^+$ , dissolved  $\text{O}_2$  and HTO in saturated  
 55 CEM I cement paste with respect to the capillary porosity. Different colors represent each species shown  
 56 in legend. The points are experiment data collected from references [4-17] (see detail in Appendix) and  
 57 the lines for each species are given by the best fitting.  $D_{i,0}$  is the species diffusivity in free water [18,  
 58 19]:  $D_0 = 2.2 \mu\text{m}^2/\text{ms}$  of HTO and  $\text{O}_2$ ;  $D_0 = 2.0 \mu\text{m}^2/\text{ms}$  of  $\text{Cl}^-$  and  $\text{Cs}^+$ ;  $D_0 = 1.3 \mu\text{m}^2/\text{ms}$  of  $\text{Na}^+$ .

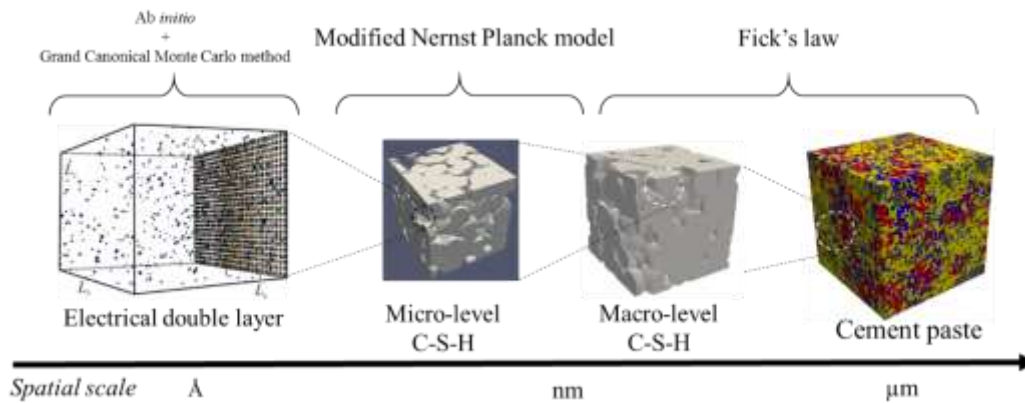
59 The surface of C-S-H carries negative charge as in contact with the high-*p*H electrolyte  
60 [20]. The ions in the pore solution interact with the charged surface and form the  
61 electrical double layer (EDL) structure near the surface depicted in Fig. 1 [21]. The  
62 bivalent calcium ions can over balance the negative charge on the surface, which cause  
63 the positive zeta potential  $\psi_d$ . This phenomenon is named as charge reversal [3]. The  
64 influence of EDL is dominant in pores of few nano-meter width and in case of  
65 compacted clays it has been reported that EDL can enhance sodium transport but reduce  
66 chloride transport [22]. Through a calibrated electronic spin resonance (ESR)  
67 experiment, the major mean sizes of gel pore are 1.8 and 7.0 nanometers [23], which is  
68 comparable with EDL thickness [24], therefore the ion-surface interaction is strong  
69 enough and the electrokinetic effect should be respected as shown by Appelo [25] and  
70 Yang & Wang [24]. However, the effect of EDL on ion transport in cement-paste is not  
71 widely studied. A collection of diffusivity of different ionic species collected from  
72 literature [4-17] (the values are tabulated in Appendix) is plotted in Fig. 2. It clearly  
73 shows that significant differences exist between relative diffusivity of different species  
74 in cement paste with diffusivity of  $\text{Cl}^-$  equal to that of uncharged tracers HTO/ $\text{O}_2$  which  
75 is higher than  $\text{Na}^+$  and  $\text{Cs}^+$  following the order  $\text{Cl}^- \square \text{HTO}/\text{O}_2 > \text{Na}^+ > \text{Cs}^+$ . These  
76 differences are significant at low capillary porosities which further strengthen the  
77 hypothesis that effect of EDL on ion transport cannot be neglected for low capillary  
78 porosities where gel pores form dominant pathway. Due to the hierarchical pore  
79 structure and complex surface chemical properties of C-S-H [26-28], to study the

80 mechanism of species diffusion in cement paste is difficult. To overcome these  
81 difficulties, the previous efforts have been taken to understand the species diffusion in  
82 C-S-H at separate scales [29-33]. At molecular scale, to quantitatively analyze the  
83 influence from surface on species diffusion, Zhou et al. [33, 34] calculated the species  
84 density distribution and mobility near the surface of C-S-H by the molecular dynamics  
85 simulation. They found that the negative charged surface caused the aggregation of  
86 calcium ions and this physical bounding effect can slow down the mobility of species.  
87 However, in terms of computation cost it is rather difficult to conduct molecular  
88 modeling simulations to investigate species diffusion in the hierarchical pore structure  
89 of C-S-H. At continuum scale, Zhang et al. [31] recently presented a multiscale pore-  
90 network approach to analyze the correlation of surface EDL with hierarchical gel pore  
91 network on the ion diffusion. Through their simulations, they demonstrated that the  
92 surface EDL effect on ion diffusivity is sensitive to pore size. However, in their  
93 modeling approach the Stern layer was considered to be non-diffusive which would  
94 result in lower diffusivity values as compared to both molecular simulations [32, 33]  
95 and experimental results [30]. This indicates that ions might be mobile in stern layer  
96 and surface steric effect slows the diffusion in the pores. One should note that the  
97 thickness of the Stern layer in C-S-H varies from 0.6 nm to 0.8 nm [31], which is  
98 significant when compared to the gel pore size. Therefore, the contribution from the  
99 Stern layer should be accounted for the transport phenomena in C-S-H phase. However,  
100 the continuum-scale modeling is difficult to deal with the ion distribution in the Stern

101 layer.

102 To provide better understanding of ion transport through multi-scale cement paste  
103 microstructure and to account for double layer effects, in this study, a multiscale  
104 modeling is proposed which combines the pore-scale modeling with the atomic-scale  
105 modeling. The multiscale approach employed in this study is depicted schematically in  
106 Fig. 3. At C-S-H scale, ion transport is modelled using pore-scale lattice Boltzmann  
107 method-based solver. Using pore-scale solver we solve a set of modified Poisson-  
108 Nernst-Planck (PNP) equations to correctly account steric effects and to provide the  
109 correction of ion concentration near surface. The modified PNP model uses the  
110 concentration and electrical potential obtained from the molecular-scale Grand  
111 Canonical Monte Carlo simulations to compute excess chemical potential which  
112 corrects the concentration profiles obtained from classical PNP model. Finally, the C-  
113 S-H diffusivity obtained is utilized to predict diffusivity of ions in cement paste. Details  
114 on multiscale framework for ion transport are presented in section 2. Following that,  
115 we validate the formulation for modified PNP model by comparing with the molecular  
116 simulations. Using the modified PNP model Section 3.1 elucidates the relationship  
117 between effective diffusivities of charged and uncharged species with pore size in a  
118 simple channel. Finally, in section 3.2 results on calculation of the effective diffusivity  
119 in virtual microstructure of C-S-H phase and cement-paste are discussed.

120



121

122 Fig. 3 Multi-scale representation of the cement paste structure and the multiscale modeling approach.

123 The molecular-level information is used to correct ion distribution within the electrical double layer. The

124 species diffusion at each scale is calculated by using the molecular simulation, the modified Nernst

125 Planck model and the Fick's law, respectively (left to right).

126

## 127 2. Multiscale modeling

### 128 2.1. Numerical regeneration of hierarchical pore structure of cement paste

129 The microstructure of cement paste exhibits a complex hierarchical structure, in which

130 pore size ranges from nanometers to micrometers [35-37]. In the past three decades,

131 different microstructure characterization techniques such as scanning electron

132 microscope, computer tomographs, neutron scattering and NMR analysis as well as

133 simulations have been employed to understand and represent the microstructure of

134 cement paste and utilize this microstructure to obtain corresponding mechanical,

135 chemical or physical properties [26, 38-41]. Since the properties of cement paste are

136 sensitive to the surrounding chemical and physical environment, direct experimental

137 measurements are difficult and it is easy to alter or even destroy the natural texture.

138 Mesoscopic modeling approaches are often used to reconstruct the cement paste texture

139 based on the observations and atomistic simulations [26, 35, 38, 42-45].

140 To have consistent representation of microstructures of cement paste from nano- to

141 micro-scale we have utilized the description provided by Bentz et al. [42]. Bentz et al.

142 [42] represented the nanoscale C-S-H structure to have two level of self-similar

143 structures: micro- and macro-level. In each level, an assembly of cluster of C-S-H

144 particles is presented by the soft spheres controlled by the hard-core-soft-shell

145 representation. At microscale, the voxel-based CEMHYD3D model (available in

146 VCCTL software [46]) is used in this study to generate the virtual microstructures of

147 cement paste. It should be noted that different descriptions have been proposed both at

148 nano- and micro-scale. For nano-scale improved colloidal models [28, 40, 43], disk

149 based packing models [47] and sheet based models [45] for C-S-H has been proposed.

150 Despite these advancements, the nanoscale pore-network of C-S-H is still unknown as

151 it is not yet possible to experimentally capture the image of C-S-H structures down to

152 the nano-scale. Similarly, at micro-scale different microstructure generation and

153 hydration models apart from CEMHYD3D exists such as HYMOSTRUC [48],  $\mu ic$  [49]

154 and HydratiCA [50]. However, the correct representation of cement paste

155 microstructure is still under debate and widely researched. Therefore, in this study we

156 have employed Bentz et al. approach due to its consistency in description of nano- and

157 micro-structure. It has been widely recognized and has been successful in explaining

158 different experimental observations.

159

## 160 2.2. Modeling ion diffusion in C-S-H

### 161 2.2.1. Monte Carlo method

162 The estimation of ion distribution in Stern layer is not straightforward. Several  
163 theoretical models have been developed to capture ion distribution in stern layer [51-  
164 55]. However, the applicability of these theoretical models for cementitious material is  
165 still not proven. Hence, in this study we utilize experimentally validated Grand  
166 Canonical Monte Carlo (GCMC) simulation of ion uptake C-S-H using the primitive  
167 model of electrolyte to obtain ion distribution in stern layer [56]. The GCMC simulation  
168 can be viewed as one-dimensional setup, which provides equilibrium concentration and  
169 potential distribution profiles near C-S-H surface. The simulation domain for GCMC  
170 consists of a box with C-S-H surface at one end as shown in Fig. 1. The surface charged  
171 density of C-S-H surface depends on the  $pH$  value and is calculated from the ab initio  
172 simulations which indicate that the surface of C-S-H can be represented by titrating  
173 surface sites  $>SiOH$  with the site density  $2.4 \text{ sites/nm}^2$ . The sites are distributed in pairs  
174 according to the crystal structure of tobermorite. The solvent of the pore solution is  
175 approximated by a dielectric continuum with the permittivity  
176  $\varepsilon = \varepsilon_r \varepsilon_0 = 6.95 \times 10^{-10} \text{ C}^2 / \text{J} \cdot \text{m}$ . The ions in the solution are represented by hard  
177 spheres with the same radius 0.2 nm.

178 The Monte Carlo simulation provides equilibrium concentration profiles of ions  
179  $C_i^{GCMC}(x)$ . The mean electrostatic potential at the distance  $x$  to the surface is obtained  
180 by integrating the charge density distribution  $\rho_e(x) = \sum_i z_i C_i^{GCMC}(x)$ :

181 
$$\psi^{GCMC}(x) = -\frac{1}{\varepsilon_r \varepsilon_0} \int_x^\infty (t-x) \rho_e(t) dt. \quad (1)$$

182 Note that above equation is obtained by integration of the Poisson equation. Finally,  
 183 this molecular simulation presents the one-dimensional concentration and potential  
 184 distributions away from the C-S-H surface in each situation.

### 185 2.2.2. Governing equations for ion transport at pore-scale

#### 186 ● Ion transport in micro-level C-S-H

187 Ion transport at the pore scale in the micro-level C-S-H can be described using the  
 188 Poisson-Nernst-Planck (PNP) equations [24, 57] given as:

189 
$$\frac{\partial C_i}{\partial t} + \nabla \cdot \mathbf{J}_i = 0, \quad (2)$$

190 
$$\mathbf{J}_i = -D_{i,0} \nabla C_i - D_{i,0} \frac{z_i e C_i}{kT} \nabla \psi, \quad (3)$$

191 where  $C_i$ ,  $D_{i,0}$ ,  $\mathbf{J}_i$  and  $z_i$  denotes the aqueous concentration (mol/m<sup>3</sup>), diffusion  
 192 coefficient in free water (m<sup>2</sup>/s), flux (mol/m<sup>2</sup>/s) and valence of the  $i^{\text{th}}$  species,  
 193 respectively.  $t$  is time (s),  $e$  the absolute charge of electron (C),  $k$  the Boltzmann  
 194 constant (J/K) and  $T$  the absolute temperature (K). In the above equation the local  
 195 electrical potential  $\psi$  (V) is obtained from the following Poisson equation:

196 
$$\nabla^2 \psi = -\frac{\rho_e}{\varepsilon_r \varepsilon_0} = -\sum_i \frac{N_A e z_i C_i}{\varepsilon_r \varepsilon_0}, \quad (4)$$

197 where  $\rho_e$  is the net charge density (C/m<sup>3</sup>) and  $N_A$  the Avogadro's number (mol<sup>-1</sup>).  
 198 Equations (3) and (4) are derived under the assumption that ions in electrolyte are  
 199 considered as charge points ignoring their volumetric effects. Therefore, equations (3)  
 200 and (4) are valid only under dilute conditions [58]. In order to account for steric effects,

201 the modification to classical PNP model is proposed. To derive the modified PNP model  
 202 it is assumed that since the charge balance within EDL is extremely rapid [59] and the  
 203 ion near C-S-H surface is in chemical quasi-equilibrium state. Under this condition, the  
 204 chemical potential must be equal in the Stern layer, diffuse layer and bulk solution [53]:

$$205 \quad kT \ln(a_{i,\infty}) = kT \ln(a_i(x)) + z_i e \psi(x) + \hat{\mu}_i^{ex}, \quad (5)$$

206 where  $a_{i,\infty}$  and  $a_i$  are the activity of  $i^{\text{th}}$  species in the bulk solution and EDL,  
 207 respectively. In equation (5), an excess term  $\hat{\mu}_i^{ex}$  is added to the classical chemical  
 208 potential, caused by the steric effect and ion-ion correlation. Considering  $a_i = \gamma_i C_i$ , we  
 209 have:

$$210 \quad kT \ln(C_{i,\infty}) = kT \ln(C_i(x)) + z_i e \psi(x) + \left( \hat{\mu}_i^{ex} + kT \ln\left(\frac{\gamma_i(x)}{\gamma_{i,\infty}}\right) \right) \\
 = kT \ln(C_i(x)) + z_i e \psi(x) + \mu_i^{ex} \quad (6)$$

211 This excess chemical potential  $\mu_i^{ex}$  should be near zero within diffuse layer or free  
 212 water. The flux in the Nernst-Planck equation is modified as follows:

$$213 \quad \mathbf{J}_i = -D_{i,0} \nabla C_i - D_{i,0} \frac{z_i e C_i}{kT} \nabla \psi - D_{i,0} \frac{C_i}{kT} \nabla \mu_i^{ex}. \quad (7)$$

214 The boundary condition for ion diffusion on the solid-liquid interface is the non-flux  
 215 boundary condition and for potential is the constant electrical potential (Dirichlet  
 216 boundary condition).

217 According to equations (5), the concentration with respect to the distance  $x$  away from  
 218 charged surface follows:

$$219 \quad \frac{C_i(x)}{C_{i,\infty}} = \exp\left(-\frac{e z_i}{kT} \psi(x) - \frac{1}{kT} \mu_i^{ex}(x)\right), \quad (8)$$

220 and therefore, the dimensionless excess chemical potential  $\mu_i^{ex} / kT$  in the Stern layer  
 221 along the direction perpendicular to surface of C-S-H is given by:

$$222 \quad \frac{1}{kT} \mu_i^{ex}(x) = -\frac{ez_i}{kT} \psi^{GCMC}(x) - \ln\left(\frac{C_i^{GCMC}(x)}{C_{i,\infty}}\right). \quad (9)$$

223 Substituting the distributions  $C_i^{GCMC}(x)$  and  $\psi^{GCMC}(x)$  obtained from the Grand  
 224 Canonical Monte Carlo method into equation (9) we get the distribution of  $\mu_i^{ex} / kT$   
 225 in the Stern layer, which is then fitted with a nonlinear function  $F(x, C_{i,\infty})$  to get the  
 226 relationship of  $\mu_i^{ex} / kT$  with respect to the distance  $x$  and bulk concentration  $C_{i,\infty}$  as:

$$227 \quad \mu_i^{ex}(x, C_{i,\infty}) / kT = F(x, C_{i,\infty}). \quad (10)$$

228 The effective diffusivity in the micro-level C-S-H is calculated by [24]:

$$229 \quad D_{i,e}^{Micro} = \frac{\int J_i dS}{S} \cdot \frac{L}{\Delta C_i}, \quad (11)$$

230 where  $\int J_i dS / S$  is the species flux per unit cross-section in the steady state,  $L$  the  
 231 medium length and  $\Delta C_i$  the mean concentration difference between two sides of the  
 232 medium.

233

234 ● **Ion transport in macro-level C-S-H and cement paste**

235 Since the mean pore size of macro-level C-S-H is large enough, the electrokinetic effect  
 236 can be ignored. The  $D_{i,e}^{Micro}$  is as input as the diffusion coefficient of solid phase in  
 237 macro-level C-S-H to get the effective diffusivities in macro-level C-S-H  $D_{i,e}^{Macro}$  by  
 238 the Fick's law:

$$239 \quad J_i = -D_{k,0} \nabla C_i, \quad (12)$$

$$D_{k,0} = \begin{cases} D_{i,0}, & \text{Pore} \\ D_{i,e}^{\text{Micro}}, & \text{Solid} \end{cases} \quad (13)$$

The effective diffusivity in the macro-level C-S-H is:

$$D_{i,e}^{\text{Macro}} = \frac{\int J_i dS}{S} \cdot \frac{L}{\Delta C_i} \quad (14)$$

### 2.2.3. Lattice Boltzmann method

Lattice Boltzmann (LB) method has shown good performances for simulating fluid flow [60, 61] and modeling multi-physical transports in porous media with complex geometries [62-64]. Benefiting its advantages for modeling transport processes in porous media, the modified Poisson-Nernst-Planck equations described in section 2.2.2 are solved using LB method. The LB solver has been optimized and implemented to run on Tesla-K80 GPGPU to provide additional speed up compared to its CPU implementation allowing use to handle large computational domains.

In this study, the SRT collision operator (with maximum value of relaxation parameter equal to one) is employed. Chai et al. [65] indicated that for relaxation time less than or equal to one the difference between SRT and MRT schemes for computing diffusion coefficient is less than 1%. Hence, SRT scheme has been chosen as it is computationally more efficient than MRT. Secondly, we choose consistent D3Q7 lattice for both diffusion and electro-kinetic potential evolution since for these processes this model is proven to be very stable and robust [24]. Moreover, it is more efficient compared to higher order lattice schemes. In the LB framework, the state of the system is evolved in terms of distribution function which corresponds to concentration  $C_i$  and potential  $\psi$

260 are [24]:

$$261 \quad f_{i,\alpha}(\mathbf{r} + c_{f_i} \delta t_{f_i} \mathbf{e}_\alpha, t + \delta t_{f_i}) - f_{i,\alpha}(\mathbf{r}, t) = -\frac{1}{\tau_{f_i}} [f_{i,\alpha}(\mathbf{r}, t) - f_{i,\alpha}^{eq}(\mathbf{r}, t)], \quad (15)$$

$$262 \quad h_\alpha(\mathbf{r} + c_h \delta t_h \mathbf{e}_\alpha, t + \delta t_h) - h_\alpha(\mathbf{r}, t) = -\frac{1}{\tau_h} [h_\alpha(\mathbf{r}, t) - h_\alpha^{eq}(\mathbf{r}, t)] + \omega_\alpha \delta t_h \frac{\rho_e}{\varepsilon_r \varepsilon_0}, \quad (16)$$

263 where  $f_{i,\alpha}$  and  $h_\alpha$  denote the distribution functions for concentration of  $i^{\text{th}}$  ion and

264 electrical potential, respectively. The equilibrium distribution functions are:

$$265 \quad f_{i,\alpha}^{eq} = \omega_\alpha C_i \left[ 1 - \frac{4D_{i,0}}{kT} \frac{\mathbf{e}_\alpha (e z_i \nabla \psi + \nabla \mu_i^{ex})}{c_{f_i}} \right], \quad (17)$$

$$266 \quad h_\alpha^{eq} = \omega_\alpha \psi, \quad (18)$$

267 where  $c_{f_i} = \delta x / \delta t_{f_i}$ .  $\delta x$  is the lattice size and  $\delta t_{f_i}$  the lattice time for  $i^{\text{th}}$  ion

268 diffusion. In D3Q7 model the distribution coefficients  $\omega_\alpha = 1/4$  for  $\alpha = 0$  and

269  $\omega_\alpha = 1/8$  for  $\alpha = 1 \sim 6$ . The discrete velocities  $\mathbf{e}_\alpha$  of D3Q7 lattice are are:

$$270 \quad \mathbf{e}_\alpha = \begin{cases} (0, 0, 0) & \alpha = 0 \\ (\pm 1, 0, 0), (0, \pm 1, 0), (0, 0, \pm 1) & \alpha = 1-6 \end{cases}. \quad (19)$$

271 The relaxation time for ion diffusion is related to the diffusion coefficient in free water

272 by  $\tau_{f_i} = 4D_{i,0} \delta t_{f_i} / \delta x^2 + 0.5$  and the relaxation time for the potential is

273  $\tau_h = 4\delta t_h / \delta x^2 + 0.5$ . The local concentration and potential are obtained from

274 distribution functions using  $C_i = \sum f_{i,\alpha}$  and  $\psi = \sum h_\alpha$ . It can be shown that the

275 above conditions, the evolution equations can recover the governing equations (2), (4)

276 and (7) using the Chapman-Enskog expansion. In the LB scheme the gradient of

277 potential can be determined by the local potential distribution functions [66] and the

278 gradient of excess potential is calculated by the difference method. The corresponding

279 numerical boundary conditions are the same as mentioned in [24]: the zero normal flux  
 280 boundary condition using ‘bounce-back’ scheme as  $f_{i,\alpha}(\mathbf{r}, t + \delta t_{f_i}) = f_{i,\beta}(\mathbf{r}, t)$ , the  
 281 constant concentration boundary condition through  
 282  $f_{i,\alpha}(\mathbf{r}, t + \delta t_{f_i}) = -f_{i,\beta}(\mathbf{r}, t) + 0.25C_{i,\infty}$  and constant potential boundary condition using  
 283  $g_{\alpha}(\mathbf{r}, t + \delta t_g) = -g_{\beta}(\mathbf{r}, t) + 0.25\psi_d$ , where the index  $\alpha$  and  $\beta$  are the opposite  
 284 directions normal to the interface.

### 285 **2.3. Calibration**

286 In this section, the modified PNP formulation is compared with the results obtained  
 287 from the GCMC simulations in order to demonstrate the use of excess potential  
 288 provides correct concentration profiles in stern layer. Additionally, comparison of  
 289 modified PNP is also made with classical PNP model to emphasis the need of modified  
 290 PNP to correctly capture ion concentrations near surface. The simulation domain  
 291 consist of the C-S-H surface at one end in contact with the pore solution consisting of  
 292  $\text{Ca}(\text{OH})_2$  electrolyte. The GCMC simulation setup consists of a three dimensional  
 293  $40 \text{ nm} \times 40 \text{ nm} \times 40 \text{ nm}$  cubic domain. The temperature is set to 298.15 K and the  
 294 absolute permittivity of the medium is set to  $6.95 \times 10^{-10} \text{ C}^2 / \text{J} \cdot \text{m}$ . The dimensionless  
 295 excess chemical potential computed using Eq. (9) as a function of distance  $x$  obtained  
 296 from GCMC is shown in Fig. 4. For lattice Boltzmann method we use a one-  
 297 dimensional domain, with length equal 100 nm and lattice spacing equal to 0.02 nm.  
 298 For modified PNP model the surface electrical potential  $\psi_0$  is used as the boundary  
 299 condition at the surface. The surface electrical potential is a function of the pH and is

300 given as  $\psi_0 = -0.0226\text{pH} + 0.0822$  (V) which is obtained from GCMC simulation.

301 Zeta potential ( $\psi_d$ ) equals to 20 mV [31] used as boundary condition near the surface

302 for classical PNP model. Zeta potential is defined at the location of the slipping plane

303 near the interface between the Stern layer and the diffuse layer and in this study the

304 position of slipping plane is assigned to be one and a half ion diameter (0.6 nm) from

305 the surface. The equilibrium potential and ion distributions with respect to the distance

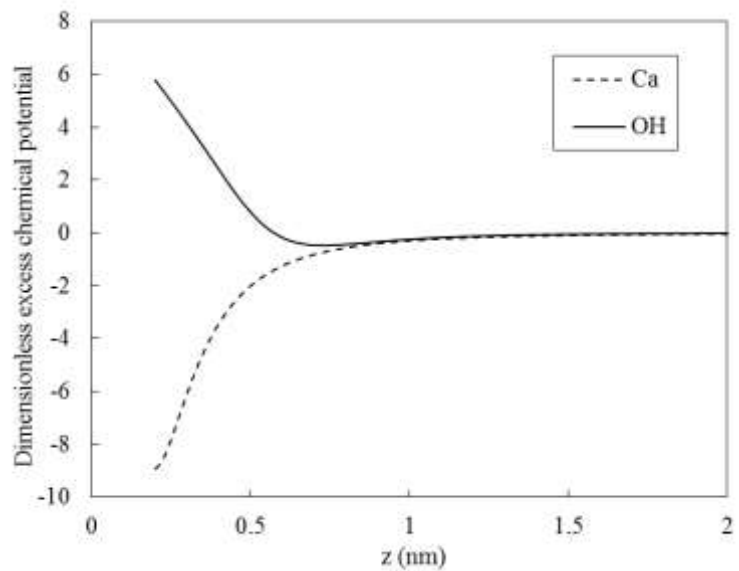
306 away from C-S-H surface obtained from classical PNP model and the modified PNP

307 model are plotted in Fig. 5. It is clear that near the surface classical PNP model

308 significantly over predicts the ion concentration for both calcium and hydroxyl ions

309 compared to the modified model and GCMC simulations.

310



311

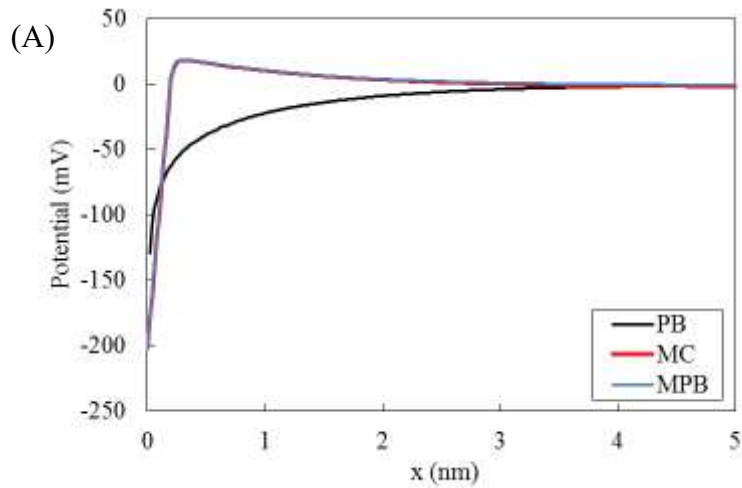
312 Fig. 4 The dimensionless excess chemical potential  $\mu_i^{ex}/kT$  obtained by the Monte Carlo simulation as

313 a function of distance away from C-S-H surface. The dashed line is the calcium ion and the solid hydroxyl

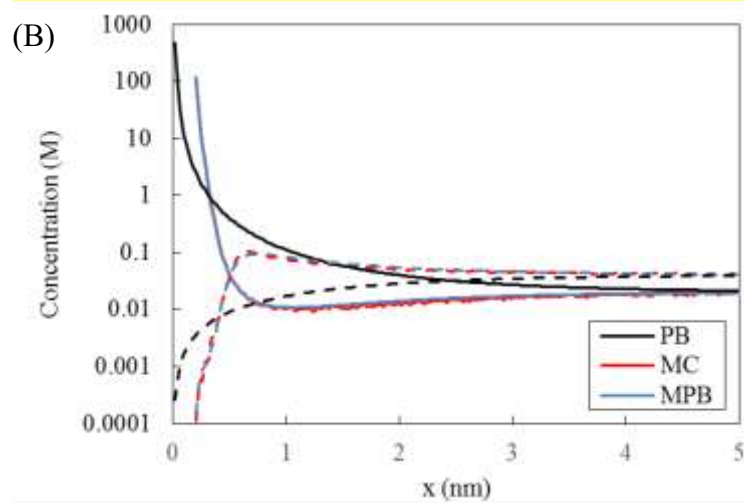
314 ion. The charged surface is set at  $z = 0$  and as far away from surface the value of  $\mu_i^{ex}/kT$  is near zero.

315 The pH is 12.5 and the bulk concentration of  $\text{Ca}(\text{OH})_2$  is  $20 \text{ mol/m}^3$ .

316



317



318

319 Fig. 5 The electrical potential (A) and ion concentration distribution (B) with respect to the distance  $x$   
 320 normal to the C-S-H surface. The red lines are from the Monte Carlo simulation from [56], blue lines  
 321 modified PNP model (MPB) and black lines classical PNP model (PB). In figure (B), the dash line  
 322 denotes hydroxide ion and solid calcium ion. In C-S-H, the thickness of Stern layer for classical PNP  
 323 model is set as 0.6 nm [56].

324

### 325 3. Results and discussion

326 In this section the proposed multiscale modeling approach has been utilized to first  
 327 obtain effective diffusion of charged species in a single C-S-H pore to investigate  
 328 systematically the effect of pore-size on effective diffusivity. Later the model is applied  
 329 to obtain the effective diffusivity from hierarchical C-S-H structure and cement paste

330 microstructure. The pore solution in simulation is simplified as a mixture of  $\text{Ca}(\text{OH})_2$   
331 and  $\text{NaCl}$  with  $\text{pH} = 12.5$  and the temperature set to 298.15 K. Due to the constant  $\text{pH}$   
332 and temperature, the surface of C-S-H is assumed to be homogeneous charged. Results  
333 obtained from modified PNP equation are also compared with classical PNP model to  
334 highlight the impact of stern layer on effective diffusivity which has been considered  
335 to be non-diffusive in previous studies [20, 24, 31]. For the classical PNP model, the  
336 Stern layer is assumed to be immobile, and zeta potential is set as 20 mV as mentioned  
337 before. The stern layer thickness is assumed to be 1.5 layers of hydrated ion which is  
338 equal to 0.6 nm. The first layer of hydrated ions in stern layer consist of calcium ion  
339 which has very low mobility due to strong bonding of bivalent ion to the surface as  
340 reported in literature based on molecular dynamic simulations[67-69]. Therefore, for  
341 modified PNP model the first adsorbed layer of Stern layer is considered non-diffusive.  
342 However, the ions in the second adsorbed layer are mobile in case of modified PNP  
343 model. For simplification same diffusion coefficient  $1 \times 10^{-9} \text{ m}^2/\text{s}$  is used for all  
344 species in free water.

345

### 346 **3.1. Diffusivity in single pore**

347 The simulation domain for single pore consists of a two-dimensional straight channel  
348 with two reservoirs as shown in Fig. 6. The width of channel  $w$  is changed from 1.0 nm  
349 to 20 nm to mimic different pore size and porosity of the system is kept equal to 0.5 by  
350 maintaining constant ratio for channel width to vertical domain width  $w/H$  as 0.5. The

351 lattice spacing is set to 0.1 nm. The surface electrical potential is set to -0.205 V  
 352 corresponding to pH equal to 12.5. For the inlet/outlet boundary conditions, we set a  
 353 zero electrical potential and fixed concentration for each ion. For all other directions  
 354 periodic boundary conditions are applied. The concentration of  $\text{Ca}(\text{OH})_2$  at inlet and  
 355 outlet is set to the same value of  $20 \text{ mol/m}^3$ . The concentration of HTO at inlet is set as  
 356  $20.5 \text{ mol/m}^3$  and  $19.5 \text{ mol/m}^3$  at outlet. Two mean concentrations of NaCl ( $10 \text{ mol/m}^3$   
 357 and  $100 \text{ mol/m}^3$ ) are adopted to investigate how the NaCl concentrations affect the  
 358 effective diffusion coefficient, and the normalized concentration difference  
 359  $(C_{\text{inlet},i} - C_{\text{inlet},i}) / C_i$  is equal to 0.1. The values of concentration boundary conditions of  
 360 NaCl at inlet and outlet are listed in Table 1.

361

362 Table 1 Concentration boundary conditions of NaCl at inlet and outlet for simulation

	Mean concentration	
	$10 \text{ mol/m}^3$	$100 \text{ mol/m}^3$
Inlet concentration ( $\text{mol/m}^3$ )	10.5	105
Outlet concentration ( $\text{mol/m}^3$ )	9.5	95

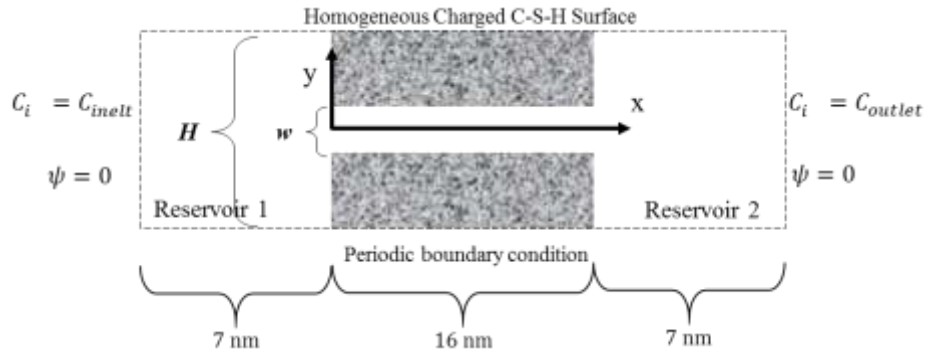
363

364 The normalized effective diffusivity with respect to the pore size shows a complex  
 365 nonlinear relationship as shown in Fig. 7. For instance, the normalized effective  
 366 diffusivity of chloride ion reaches the peak as the channel width is 2 nm and quickly  
 367 drops below this width. The normalized effective diffusivities of HTO and sodium, in  
 368 contrast, always decrease when the channel width is reduced. For channel widths larger

369 than 1.2 nm the effective diffusivity of chloride is larger than for sodium and HTO.  
370 However, for small pores ( $\leq 1.2$  nm), since the Stern layer mainly occupies the pore  
371 space it is difficult for negative charged species to access the pores, and therefore, HTO  
372 effective diffusivity is higher than that of chloride ion. To quantify the applicability of  
373 classical PNP model for each species, it assumed that when the relative difference  
374 between classical PNP model and modified PNP model is less than 20% it is considered  
375 to be valid. For chloride and HTO the classical PNP model is found to be valid for pore  
376 size larger than 3 nm. However, due to the complex electrical adsorption (physical  
377 adsorption) of sodium ion in the Stern layer the classical PNP model is only valid for  
378 pore size larger than 20 nm. The surface of C-S-H is negative charged and the  
379 concentration of chloride ions are higher than sodium ions in diffuse layer due to the  
380 charge reversal (shown in Fig. 1). This is the main reason why the effective diffusivity  
381 of chloride ion is larger than that of sodium ion. As a result, when the channel width is  
382 less than 3 nm, the contribution from Stern layer cannot be ignored and the classical  
383 PNP model will underestimate the effective diffusivity. For channel widths larger than  
384 20 nm the EDL effect vanishes for all species. Fig. 9 shows the effective diffusion  
385 coefficients calculated by the modified PNP model with NaCl concentration of 10  
386 mol/m<sup>3</sup> and 100 mol/m<sup>3</sup>. Due to the constant *pH* value of pore solution, the surface  
387 charge density is constant for both concentrations. As the surface charge in C-S-H is  
388 mainly balanced by the calcium ions, the sodium ion does not significantly alter the  
389 thickness of EDL. Therefore, although the concentration of NaCl changes one order the

390 effective diffusion coefficients in C-S-H of sodium and chloride ions hardly varies.

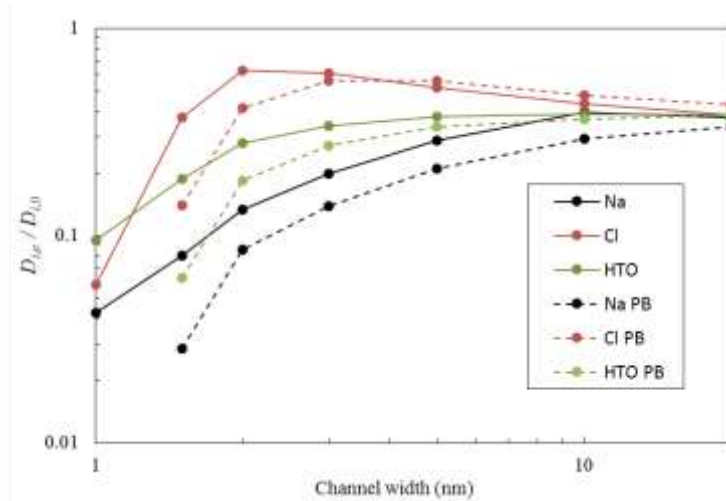
391



392

393 Fig. 6 The simulation domain of simple two-dimensional channel and corresponding boundary  
 394 conditions. The width of channel  $w$  changes from 1 nm to 20 nm and  $w/H$  is constant as 0.5.

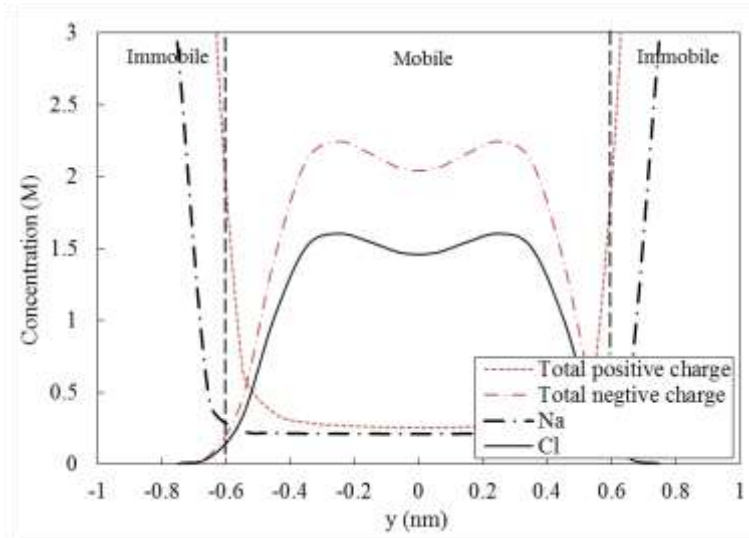
395



396

397 Fig. 7 Normalized effective diffusion coefficients of  $\text{Na}^+$ ,  $\text{Cl}^-$  and HTO with respect to widths of channel.  
 398 The solid lines are calculated by our modified PNP model and dash lines are from classical PNP model  
 399 (PB). Red denotes chloride ion, green HTO and black sodium ion.  $\text{NaCl}$  concentration is  $10 \text{ mol/m}^3$  and  
 400  $\text{Ca(OH)}_2$   $20 \text{ mol/m}^3$ .

401



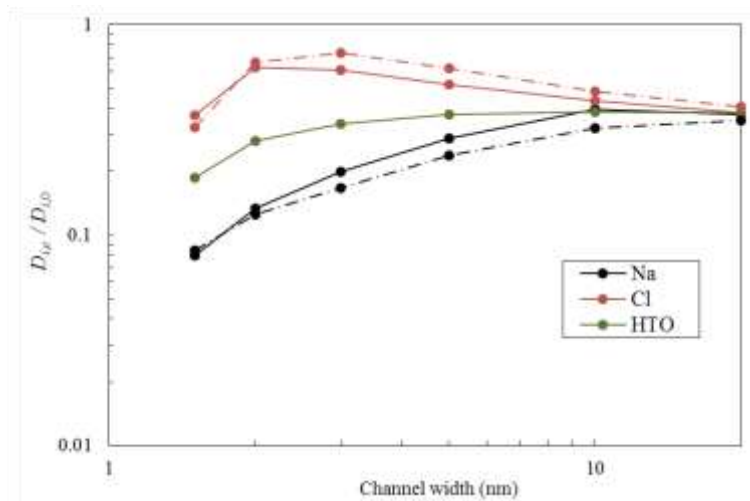
402

403 Fig. 8 The concentration distribution of middle cross section in 2D channel by the present simulation.

404 The width of channel is 2 nm. The charged C-S-H surface is in  $\pm 1$  nm and the first-adsorbed layer is

405 immobile.

406



407

408 Fig. 9 Normalized effective diffusion coefficients of  $\text{Na}^+$ ,  $\text{Cl}^-$  and HTO with respect to ion concentration.

409 We use two concentrations of NaCl  $100 \text{ mol/m}^3$  and  $10 \text{ mol/m}^3$  but the same concentration  $20 \text{ mol/m}^3$

410 for  $\text{Ca}(\text{OH})_2$ . The solid lines are calculated by using  $100 \text{ mol/m}^3$  NaCl and dash-point lines  $10 \text{ mol/m}^3$

411 NaCl. Red denotes chloride ion, green HTO and black sodium ion.

412

### 413 3.2. Effective diffusivity from virtual cement microstructures

414 In this section, in order to compare modeling results with the experiment data shown in

415 Fig. 2 the effective diffusion coefficients in C-S-H  $D_{i,e}^{\text{C-S-H}}$  are first calculated in section

416 3.2.1 and  $D_{i,e}^{C-S-H}$  are then used to predict the effective diffusivities in cement paste in

417 section 3.2.2.

### 418 3.2.1. Effective diffusivity in C-S-H phase

419 For the micro-level C-S-H structures, the solid is non-diffuse and the surface is

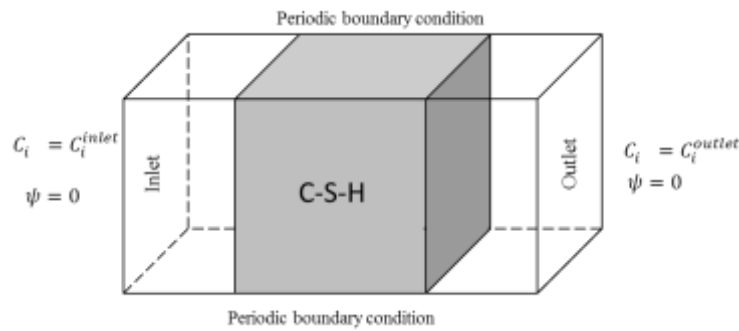
420 homogeneous charged. The surface electrical potential is -0.21 V at pH=12.5. However,

421 in macro-level C-S-H structures, the solid phase is diffusive and the diffusion

422 coefficient of the solid phase is set to the one obtained from micro-level C-S-H structure

423 by changing the relaxation time in LB scheme.

424



425

426 Fig. 10 The simulation domain of C-S-H phase and corresponding boundary conditions.

427

428 For the regenerated micro-level C-S-H structure, the porosity is 22.3% and the mean

429 pore size is 1.59 nm computed by the maximum sphere algorithm [70]. Within these

430 narrow pores EDL effects cannot be ignored and the classical PNP model is not valid.

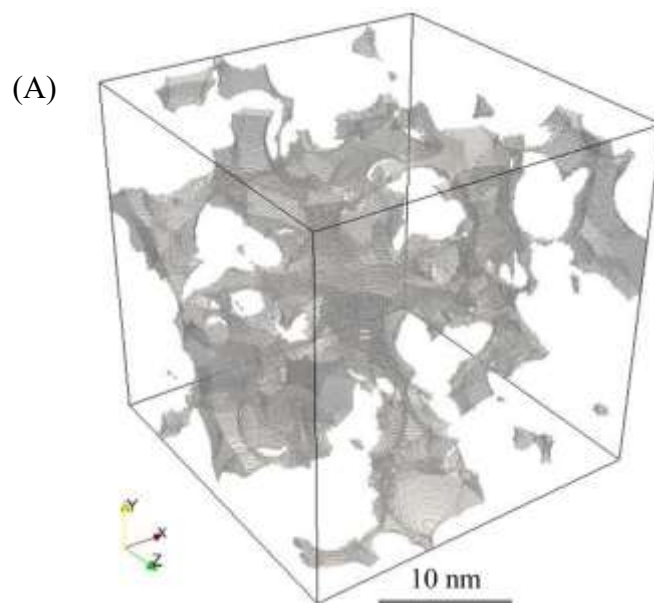
431 Therefore, the modified PNP model proposed in this study has been used to calculate

432 the effective diffusivity  $D_{i,e}^{Micro}$  in the regenerated micro-level C-S-H microstructures.

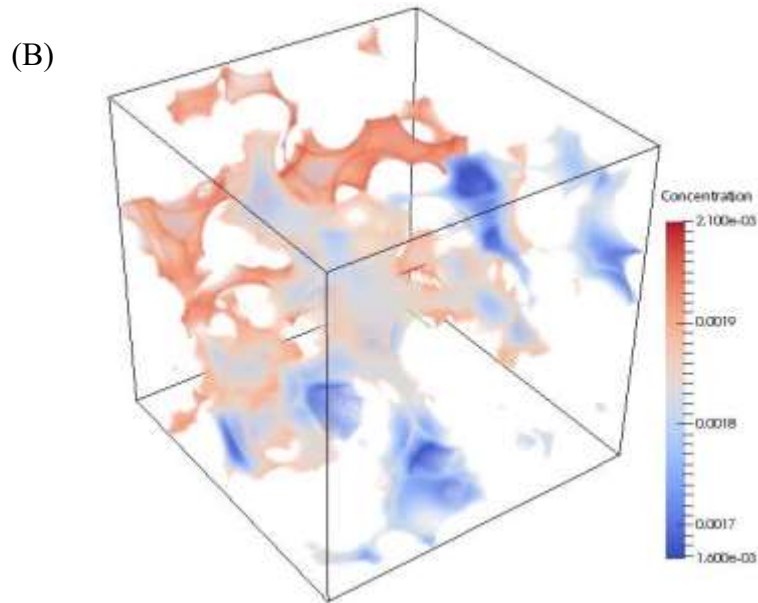
433 The size of the three-dimensional simulation domain is 32.5 nm × 25 nm × 25 nm

434 meshed by a uniform  $260 \times 200 \times 200$  grid. The boundary conditions are shown in Fig.  
435 10 and the average concentrations of  $\text{Ca}(\text{OH})_2$  and  $\text{NaCl}$  are 20 mM and 10mM,  
436 respectively. Fig. 11 shows micro-level C-S-H pore space generated for the three-  
437 dimensional simulations and the corresponding steady-state chloride ion concentration  
438 distribution in the pore space. The effective diffusivity in the macro-level C-S-H is  
439 calculated by the Fick's law. The simulation domain of macro-level C-S-H is  $325 \text{ nm} \times$   
440  $250 \text{ nm} \times 250 \text{ nm}$  with the lattice spacing equal to 1.25 nm. The normalized effective  
441 diffusion coefficients are shown in Table 2.

442



443



444 Fig. 11 (A) Visualization of gel pores regenerated by the Bentz et al. method [42] and (B) the steady  
 445 distribution of chloride ion concentration in micro-level C-S-H are shown. The solid phase is hyaline and  
 446 invisible. Stochastic characteristics are very clear for the ion concentration across one section.  
 447

448

449 Table 2 Normalized effective diffusion coefficients of  $\text{Na}^+$ ,  $\text{Cl}^-$  and HTO in micro- and macro-level C-S-  
 450 H

Normalized Effective diffusivity*	$\text{Na}^+$	$\text{Cl}^-$	HTO
<i>Micro-level C-S-H</i> $D_{i,e}^{\text{Micro}} / D_{i,0}$	0.00871	0.0259	0.0244
<i>Macro-level C-S-H</i> $D_{i,e}^{\text{Macro}} / D_{i,0}$	0.0244	0.0455	0.0438

451 \* The effective diffusivities are normalized by the diffusion coefficients in the free water  $D_{i,0}$ .

452

### 453 3.2.2. Effective diffusivity in cement paste

454 The virtual microstructures of cement paste are obtained using CEMHYD3D (available  
 455 in VCCTL software). The standard cement material “cement 140” from the VCCTL

456 material library is used and the detail of component is shown Table 3. The water-cement

457 ratios is set as 0.2, 0.3, 0.4 and 0.5, as hydration time equals to 7, 28 and 96 days. The

458 other parameters are kept as the default setting in VCCTL. The  $100\ \mu\text{m} \times 100\ \mu\text{m} \times$   
 459  $100\ \mu\text{m}$  virtual microstructures of cement paste are used as the simulation domain,  
 460 which is discretized using a  $100 \times 100 \times 100$  uniform regular grid. The size of  
 461 simulation domain chosen here is sufficient to have a representative elementary volume  
 462 (REV) as proven through numerical studies [2, 71, 72] and experimentally through  
 463 image technique [73]. The concentration  $2.0\ \text{mol}/\text{m}^3$  is employed as the boundary  
 464 conditions at inlet and  $1.0\ \text{mol}/\text{m}^3$  at outlet [24]. The virtual cement paste  
 465 microstructures have three type phases: capillary pores, C-S-H phase and other solid  
 466 phases. Other solid phases include hydration phases other than C-S-H and unhydrated  
 467 clinkers which are treated as non-diffusive. Ion diffusivity in capillary pores is assumed  
 468 to be identical to diffusivity in free water.

469

470 Table 3 The major phase volume fractions of “cement 140” in VCCTL used in study.

C <sub>3</sub> S	C <sub>2</sub> S	C <sub>3</sub> A	C <sub>4</sub> AF
0.6576	0.180	0.0994	0.0633

471

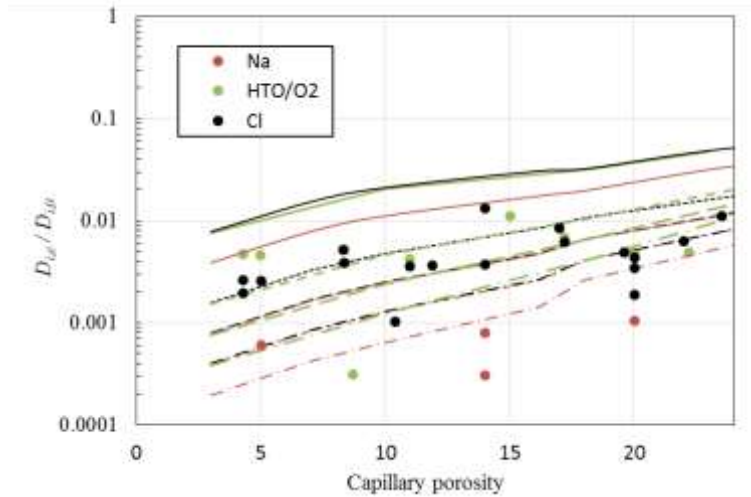
472 Simulations in previous sections have been carried out under the assumption that the  
 473 local mobility of each species in the C-S-H is the same as in the free water. However  
 474 due to the electro viscosity and steric effects near the surface, the molecular dynamic  
 475 simulations [32, 34, 74, 75] has shown that the ions in gel pores of C-S-H has only 25%  
 476 -50% percent mobility than that in the free water. The quasi-elastic neutron scattering

477 (QENS) experiments [30] also suggested that the water in gel pores diffuses slowly  
478 ( $\sim 10^{-10} \text{ m}^2\text{s}^{-1}$ ). Moreover, the colloidal representation of C-S-H developed by Bentz  
479 [42] may not give correct pore size distribution and as a result the model connectivity  
480 might be much higher than that of the real C-S-H structures. Therefore, in this study,  
481 the effective diffusivity in C-S-H  $D_{i,e}^{\text{C-S-H}}$  is determined by:

$$482 \quad D_{i,e}^{\text{C-S-H}} = D_{i,e}^{\text{Macro}} / \delta_D, \quad (20)$$

483 where  $\delta_D$  is the attenuation factor to indicate slow-down degree of mobility in gel  
484 pores of C-S-H. The effective diffusivities of species in cement paste are calculated by  
485 equation (14). A parametric study has been carried out to roughly identify the  
486 attenuation factor for ionic mobility within gel pores [30, 34] by varying it from 5 to 20  
487 shown in Fig. 12. Fig. 12 compares the effective diffusivities obtained from simulations  
488 with experiment data presented in Fig. 2. If  $\delta_D = 1$ , the effective diffusivity computed  
489 is higher than the experimental values. The parametric study reveals that the value of  
490 the attenuation factor  $\delta_D$  for chloride ion and HTO should be around 5~10 and for  
491 sodium ion around 20. It means that the local mobility in C-S-H has a significant  
492 influence on mass transport in confined nanopores of cement paste and the better  
493 representation of the C-S-H pore-structure is needed.

494



495  
 496 Fig. 12 Comparison of calculated and experimentally measured effective diffusion coefficients. Points  
 497 are the diffusion coefficients by experimental measurement collected from references [4-17] (see detail  
 498 in Appendix) and solid lines are from our simulations by using the attenuation factor  $\delta_d = 1$ ; dotted lines  
 499 are  $\delta_d = 5$ ; dashed lines  $\delta_d = 10$ ; dotted-dashed lines  $\delta_d = 20$ .  
 500

## 501 4. Conclusions

502 The goal of this study was to quantify the charged or non-charged transport in cement  
 503 paste microstructure accounting for EDL effects near charged C-S-H surface. To  
 504 achieve this goal a multiscale modeling framework has been presented which combines  
 505 Grand canonical Monte Carlo simulation at molecular scale with the lattice Boltzmann  
 506 method at pore scale. The proposed methodology is first applied to investigate effect of  
 507 pore-size on species transport and later applied to obtain effective diffusivity of C-S-H.  
 508 The C-S-H diffusivity obtained has been utilized as an input at cement paste scale to  
 509 predict effective diffusivity in microstructures of cement paste. A coupling between  
 510 pore scale modeling approach and molecular modeling approach can be successfully  
 511 achieved using the proposed modified PNP model thus bridging the scale gap between

512 the two models. The effective diffusivity with respect to pore size shows a complex  
513 nonlinear relationship. For a simple channel geometry, the classical PNP model  
514 compares well with the modified PNP model for chloride ion and HTO as long as the  
515 width of channel is larger than 3 nm. The classical PNP model is not applicable to  
516 describes sodium ion diffusion for pore size smaller than 20 nm. When the pore-size is  
517 smaller than 3 nm, the influence of steric and ion-ion correlation effects is important  
518 and the classical PNP model significantly over predicts the concentrations near surfaces.  
519 At pore size around 2 nm the effective diffusivity of chloride ions has the peak value,  
520 whereas the normalized effective diffusivity of HTO and sodium ion increases with  
521 increase in the pore size.

522 Simulations presented in this study shows that the effective diffusion coefficient of  
523 chloride ion in C-S-H is similar to that of HTO, but much larger than the sodium ion.  
524 At cement paste scale, our model qualitatively captures the effects of electrical double  
525 layer on diffusivity as reported experimentally. We found that in order to match  
526 experiment data the model needs to include attenuation factors of 5-20. We relate this  
527 partially to the poor description of hierarchical pore structure of cement paste and  
528 partially to the unknown local mobility within gel pores near surface which can be  
529 quantified in future using molecular dynamic simulations.

530

531 **Appendix**

532 The relative effective diffusion coefficients of Na<sup>+</sup>, Cl<sup>-</sup>, Cs<sup>+</sup>, dissolved O<sub>2</sub> and HTO in  
 533 saturated CEM I cement paste with respect to the capillary porosity collected from  
 534 different references.

Species	Normalized diffusivity $D_{i,c}/D_{i,0}$	Water/cement ratio	Hydrated time (days)	Degree of hydration <sup>‡</sup>	Porosity	Ref.
Chloride	0.00123	0.4	7	0.6	25*	[5]
	0.00270	0.4	7	0.6	25*	
	0.00344	0.4	28	0.7	20*	[4]
	0.0133	0.3	7	0.6	14*	
	0.00435	0.4	28	0.7	20*	
	0.00369	0.35	28	0.7	14*	[6]
	0.0111	0.4	28	0.7	23.5	
	0.00635	0.35	28	0.7	22	
	0.00403	0.4	7	0.6	26*	[8]
	0.00187	0.4	28	0.7	20*	[10]
	0.00354	0.35	56	0.76	11*	[12]
	0.00254	0.25	56	0.76	5*	
	0.00194	0.4	84	0.79	4.3	[13]
0.00389	0.5	84	0.79	8.36		

	0.00620	0.6	84	0.79	17.18
	0.0105	0.7	84	0.79	24.86
	0.00475	0.4	28	0.7	20* [10]
	0.00465	0.4	84	0.79	4.3
Oxygen	0.00520	0.5	84	0.79	8.36 [13]
	0.00682	0.6	84	0.79	17.18
	0.0108	0.7	84	0.79	24.86
	0.00491	0.45	21	0.68	22.2 [9]
Tritiated	0.00420	0.35	56	0.76	11* [12]
water	0.00455	0.35	56	0.76	5*
	0.0110	0.35			15 [76]
	0.000188	0.4	7	0.6	25* [5]
	0.000601	0.3	84	0.76	5*
	0.00105	0.4	28	0.7	20* [4]
Sodium	0.000308	0.35	28	0.7	14*
	0.000789	0.3	7	0.6	14*
	0.00105	0.4	7	0.6	26* [8]
	0.00000073	0.2	7	0.6	3*
Cesium	0.0000731	0.3	7	0.6	13* [16]
	0.000487	0.4	7	0.6	25*

0.001463	0.5	7	0.6	34*
0.000112	0.4	28	0.7	20*
				[6]
0.0000790	0.35	28	0.7	14
0.000419	0.4	28	0.7	23.5
				[7]
0.000253	0.35	28	0.7	22*
0.000878	0.4	7	0.6	26* [15]
0.000575	0.4	28	0.7	20* [17]
0.00117	0.42	28	0.7	22*
				[14]
0.00419	0.42	28	0.7	22*
0.000536	0.35	56	0.76	11*
				[12]
0.000375	0.25	56	0.76	5*

535 \* The porosity is predicted by the Power's model.

536 ‡ The degree of hydration is taken as suggested by Hansen [77].

537

## 538 **Acknowledgement**

539 Y. Yang and M. Wang acknowledges financial support by the NSF grant of China

540 (No.51766107). Y. Yang acknowledges the financial support by China Scholarship

541 Council's (CSC) Chinese Government Graduate Student Overseas Study Program. R.

542 Patel acknowledges funding received from the European Union's Horizon 2020

543 research and innovation programme under the Marie Skłodowska-Curie grant

544 agreement No 701647.

545

## 546 Reference

- 547 [1] E.J. Garboczi, D.P. Bentz, Modelling of the microstructure and transport properties  
548 of concrete, *Construction and Building Materials* 10(5) (1996) 293-300.
- 549 [2] R.A. Patel, J. Perko, D. Jacques, G. De Schutter, G. Ye, K. Van Bruegel, Effective  
550 diffusivity of cement pastes from virtual microstructures: Role of gel porosity and  
551 capillary pore percolation, *Construction and Building Materials* 165 (2018) 833-845.
- 552 [3] C. Labbez, A. Nonat, I. Pochard, B. Jonsson, Experimental and theoretical evidence  
553 of overcharging of calcium silicate hydrate, *J. Colloid Interface Sci.* 309(2) (2007) 303-  
554 7.
- 555 [4] S. Goto, D.M. Roy, Diffusion of ions through hardened cement pastes, *Cem. Concr.*  
556 *Res.* 11(5) (1981) 751-757.
- 557 [5] S. Chatterji, Transportation of ions through cement based materials. Part 3  
558 experimental evidence for the basic equations and some important deductions, *Cem.*  
559 *Concr. Res.* 24(7) (1994) 1229-1236.
- 560 [6] A. Kumar, B. Roy, Retardation of Cs<sup>+</sup> and Cl<sup>-</sup> diffusion using blended cement  
561 admixtures, *J. Am. Ceram. Soc.* 69(4) (1986) 356-360.
- 562 [7] A. Kumar, S. Komarneni, D.M. Roy, Diffusion of Cs<sup>+</sup> and Cl<sup>-</sup> through sealing  
563 materials, *Cem. Concr. Res.* 17(1) (1987) 153-160.
- 564 [8] S. Chatterji, M. Kawamura, Electrical double layer, ion transport and reactions in  
565 hardened cement paste, *Cem. Concr. Res.* 22(5) (1992) 774-782.
- 566 [9] A. Delagrave, J. Marchand, M. Pigeon, Influence of Microstructure on the Tritiated  
567 Water Diffusivity of Mortars, *Advanced Cement Based Materials* 7(2) (1998) 60-65.
- 568 [10] M. Castellote, C. Alonso, C. Andrade, G.A. Chadbourn, C.L. Page, Oxygen and  
569 chloride diffusion in cement pastes as a validation of chloride diffusion coefficients  
570 obtained by steady-state migration tests, *Cem. Concr. Res.* 31(4) (2001) 621-625.
- 571 [11] J. Tits, A. Jakob, E. Wieland, P. Spieler, Diffusion of tritiated water and <sup>22</sup>Na<sup>+</sup>  
572 through non-degraded hardened cement pastes, *J. Contam. Hydrol.* 61(1-4) (2003) 45-  
573 62.
- 574 [12] H.M. Johnston, D.J. Wilmot, Sorption and diffusion studies in cementitious grouts,  
575 *Waste Manage.* 12(2-3) (1992) 289-297.
- 576 [13] V.T. Ngala, C.L. Page, L.J. Parrott, S.W. Yu, Diffusion in cementitious materials:  
577 II, further investigations of chloride and oxygen diffusion in well-cured OPC and  
578 OPC/30%PFA pastes, *Cem. Concr. Res.* 25(4) (1995) 819-826.
- 579 [14] K.G. Papadokostaki, A. Savidou, Study of leaching mechanisms of caesium ions  
580 incorporated in Ordinary Portland Cement, *J. Hazard. Mater.* 171(1-3) (2009) 1024-31.
- 581 [15] A. Atkinson, A.K. Nickerson, Diffusion and Sorption of Cesium, Strontium, and  
582 Iodine in Water-Saturated Cement, *Nucl. Technol.* 81(1) (1988) 100-113.
- 583 [16] A. Atkinson, A.K. Nickerson, The diffusion of ions through water-saturated cement,  
584 *Journal of Materials Science* 19(9) (1984) 3068-3078.
- 585 [17] M. Castellote, C. Andrade, C. Alonso, Characterization of transport of caesium,

586 strontium, cobalt and iron ions through concrete by steady-state migration and natural  
587 diffusion tests, *Advances in Cement Research* 11(4) (1999) 161-168.

588 [18] J.S. Murday, R.M. Cotts, Self - Diffusion in Liquids: H<sub>2</sub>O, D<sub>2</sub>O, and Na, *The*  
589 *Journal of Chemical Physics* 53(12) (1970) 4724-4725.

590 [19] M. Flury, T.F. Gimmi, 6.2 Solute Diffusion, in: J.H. Dane, C.G. Topp (Eds.),  
591 *Methods of Soil Analysis: Part 4 Physical Methods*, Soil Science Society of America,  
592 Madison, WI, 2002, pp. 1323-1351.

593 [20] H. Friedmann, O. Amiri, A. Aït-Mokhtar, Physical modeling of the electrical  
594 double layer effects on multispecies ions transport in cement-based materials, *Cem.*  
595 *Concr. Res.* 38(12) (2008) 1394-1400.

596 [21] C. Labbez, B. Jönsson, I. Pochard, A. Nonat, B. Cabane, Surface Charge Density  
597 and Electrokinetic Potential of Highly Charged Minerals: Experiments and Monte  
598 Carlo Simulations on Calcium Silicate Hydrate, *The Journal of Physical Chemistry B*  
599 110(18) (2006) 9219-9230.

600 [22] M.A. Glaus, S. Frick, R. Rossé, L.R.V. Loon, Comparative study of tracer diffusion  
601 of HTO, 22Na<sup>+</sup> and 36Cl<sup>-</sup> in compacted kaolinite, illite and montmorillonite, *Geochim.*  
602 *Cosmochim. Acta* 74(7) (2010) 1999-2010.

603 [23] J.P. Korb, L. Monteilhet, P.J. McDonald, J. Mitchell, Microstructure and texture of  
604 hydrated cement-based materials: A proton field cycling relaxometry approach, *Cem.*  
605 *Concr. Res.* 37(3) (2007) 295-302.

606 [24] Y. Yang, M. Wang, Pore-scale modeling of chloride ion diffusion in cement  
607 microstructures, *Cem. Concr. Compos.* 85 (2018) 92-104.

608 [25] C.A.J. Appelo, Solute transport solved with the Nernst-Planck equation for  
609 concrete pores with ‘free’ water and a double layer, *Cem. Concr. Res.* 101 (2017) 102-  
610 113.

611 [26] I.G. Richardson, The calcium silicate hydrates, *Cem. Concr. Res.* 38(2) (2008)  
612 137-158.

613 [27] S. Papatzani, K. Paine, J. Calabria-Holley, A comprehensive review of the models  
614 on the nanostructure of calcium silicate hydrates, *Construction and Building Materials*  
615 74 (2015) 219-234.

616 [28] H.M. Jennings, Refinements to colloid model of C-S-H in cement: CM-II, *Cem.*  
617 *Concr. Res.* 38(3) (2008) 275-289.

618 [29] E.J. Garboczi, D.P. Bentz, Computer simulation of the diffusivity of cement-based  
619 materials, *Journal of Materials Science* 27(8) (1992) 2083-2092.

620 [30] H.N. Bordallo, L.P. Aldridge, A. Desmedt, Water Dynamics in Hardened Ordinary  
621 Portland Cement Paste or Concrete: From Quasielastic Neutron Scattering, *The Journal*  
622 *of Physical Chemistry B* 110(36) (2006) 17966-17976.

623 [31] Y. Zhang, C. Liu, Z. Liu, G. Liu, L. Yang, Modelling of diffusion behavior of ions  
624 in low-density and high-density calcium silicate hydrate, *Construction and Building*  
625 *Materials* 155 (2017) 965-980.

626 [32] D. Hou, Z. Li, Molecular Dynamics Study of Water and Ions Transported during  
627 the Nanopore Calcium Silicate Phase: Case Study of Jennite, *J. Mater. Civ. Eng.* 26(5)

628 (2014) 930-940.

629 [33] Y. Zhou, D. Hou, J. Jiang, L. Liu, W. She, J. Yu, Experimental and molecular  
630 dynamics studies on the transport and adsorption of chloride ions in the nano-pores of  
631 calcium silicate phase: The influence of calcium to silicate ratios, *Microporous*  
632 *Mesoporous Mater.* 255 (2018) 23-35.

633 [34] Y. Zhou, D. Hou, J. Jiang, P. Wang, Chloride ions transport and adsorption in the  
634 nano-pores of silicate calcium hydrate: Experimental and molecular dynamics studies,  
635 *Construction and Building Materials* 126 (2016) 991-1001.

636 [35] I.G. Richardson, Tobermorite/jennite- and tobermorite/calcium hydroxide-based  
637 models for the structure of C-S-H: applicability to hardened pastes of tricalcium silicate,  
638  $\beta$ -dicalcium silicate, Portland cement, and blends of Portland cement with blast-furnace  
639 slag, metakaolin, or silica fume, *Cement and Concrete Research* 34(9) (2004) 1733-  
640 1777.

641 [36] M.A.B. Promentilla, T. Sugiyama, T. Hitomi, N. Takeda, Quantification of  
642 tortuosity in hardened cement pastes using synchrotron-based X-ray computed  
643 microtomography, *Cem. Concr. Res.* 39(6) (2009) 548-557.

644 [37] E. Gallucci, K. Scrivener, A. Groso, M. Stampanoni, G. Margaritondo, 3D  
645 experimental investigation of the microstructure of cement pastes using synchrotron X-  
646 ray microtomography ( $\mu$ CT), *Cem. Concr. Res.* 37(3) (2007) 360-368.

647 [38] R.J.M. Pellenq, N. Lequeux, H. van Damme, Engineering the bonding scheme in  
648 C-S-H: The ionic-covalent framework, *Cem. Concr. Res.* 38(2) (2008) 159-174.

649 [39] F. Sanchez, K. Sobolev, Nanotechnology in concrete – A review, *Construction and*  
650 *Building Materials* 24(11) (2010) 2060-2071.

651 [40] K. Ioannidou, K.J. Krakowiak, M. Bauchy, C.G. Hoover, E. Masoero, S. Yip, F.J.  
652 Ulm, P. Levitz, R.J. Pellenq, E. Del Gado, Mesoscale texture of cement hydrates, *Proc.*  
653 *Natl. Acad. Sci. U. S. A.* 113(8) (2016) 2029-34.

654 [41] B. Šavija, J. Pacheco, E. Schlangen, Lattice modeling of chloride diffusion in  
655 sound and cracked concrete, *Cem. Concr. Compos.* 42 (2013) 30-40.

656 [42] D.P. Bentz, D.A. Quenard, V. Baroghel-Bouny, E.J. Garboczi, H.M. Jennings,  
657 Modelling drying shrinkage of cement paste and mortar Part 1. Structural models from  
658 nanometres to millimetres, *Materials and Structures* 28(8) (1995) 450-458.

659 [43] H.M. Jennings, A model for the microstructure of calcium silicate hydrate in  
660 cement paste, *Cem. Concr. Res.* 30(1) (2000) 101-116.

661 [44] V. Morales-Flórez, N.D. Rosa-Fox, M. Piñero, L. Esquivias, The Cluster Model:  
662 A Simulation of the Aerogel Structure as a Hierarchically-Ordered Arrangement of  
663 Randomly Packed Spheres, *J. Sol-Gel Sci. Technol.* 35(3) (2005) 203-210.

664 [45] M.A. Etzold, P.J. McDonald, A.F. Routh, Growth of sheets in 3D confinements —  
665 a model for the C-S-H meso structure, *Cem. Concr. Res.* 63 (2014) 137-142.

666 [46] J.W. Bullard, VCCTL Software, [https://www.nist.gov/services-](https://www.nist.gov/services-resources/software/vcctl-software)  
667 [resources/software/vcctl-software](https://www.nist.gov/services-resources/software/vcctl-software).

668 [47] Z. Yu, A. Zhou, D. Lau, Mesoscopic packing of disk-like building blocks in  
669 calcium silicate hydrate, *Sci. Rep.* 6 (2016) 36967.

670 [48] G. Ye, K. van Breugel, A.L.A. Fraaij, Three-dimensional microstructure analysis  
671 of numerically simulated cementitious materials, *Cem. Concr. Res.* 33(2) (2003) 215-  
672 222.

673 [49] S. Bishnoi, K.L. Scrivener,  $\mu ic$ : A new platform for modelling the hydration of  
674 cements, *Cem. Concr. Res.* 39(4) (2009) 266-274.

675 [50] W.B. Jeffrey, E. Edith, L.G. William, G.S. Steven, E.T. Judith, A parallel reaction-  
676 transport model applied to cement hydration and microstructure development, *Modell.*  
677 *Simul. Mater. Sci. Eng.* 18(2) (2010) 025007.

678 [51] J.G. Ibarra-Armenta, A. Martín-Molina, M. Quesada-Pérez, Testing a modified  
679 model of the Poisson–Boltzmann theory that includes ion size effects through Monte  
680 Carlo simulations, *Phys. Chem. Chem. Phys.* 11(2) (2009) 309-316.

681 [52] Y. Qiao, X. Liu, M. Chen, B. Lu, A Local Approximation of Fundamental Measure  
682 Theory Incorporated into Three Dimensional Poisson–Nernst–Planck Equations to  
683 Account for Hard Sphere Repulsion Among Ions, *J Stat Phys* 163(1) (2016) 156-174.

684 [53] P.M. Biesheuvel, M. van Soestbergen, Counterion volume effects in mixed  
685 electrical double layers, *J. Colloid Interface Sci.* 316(2) (2007) 490-9.

686 [54] B. Lu, Y.C. Zhou, Poisson-Nernst-Planck equations for simulating biomolecular  
687 diffusion-reaction processes II: size effects on ionic distributions and diffusion-reaction  
688 rates, *Biophys. J.* 100(10) (2011) 2475-85.

689 [55] D. Gillespie, A review of steric interactions of ions: Why some theories succeed  
690 and others fail to account for ion size, *Microfluid. Nanofluid.* 18(5-6) (2014) 717-738.

691 [56] S.V. Churakov, C. Labbez, L. Pegado, M. Sulpizi, Intrinsic Acidity of Surface Sites  
692 in Calcium Silicate Hydrates and Its Implication to Their Electrokinetic Properties, *The*  
693 *Journal of Physical Chemistry C* 118(22) (2014) 11752-11762.

694 [57] J. Arnold, D.S. Kosson, A. Garrabrants, J.C.L. Meeussen, H.A. van der Slot,  
695 Solution of the nonlinear Poisson–Boltzmann equation: Application to ionic diffusion  
696 in cementitious materials, *Cem. Concr. Res.* 44 (2013) 8-17.

697 [58] M. Wang, S. Chen, On applicability of Poisson–Boltzmann equation for micro-and  
698 nanoscale electroosmotic flows, *Commun Comput Phys* 3(5) (2008) 1087-1099.

699 [59] Y. Yang, M. Wang, Upscaling scheme for long-term ion diffusion in charged porous  
700 media, *Phys Rev E* 96(2-1) (2017) 023308.

701 [60] S. Succi, Lattice Boltzmann 2038, *EPL (Europhysics Letters)* 109(5) (2015) 50001.

702 [61] S. Chen, Z. Wang, X. Shan, G.D. Doolen, Lattice Boltzmann computational fluid  
703 dynamics in three dimensions, *J Stat Phys* 68(3-4) (1992) 379-400.

704 [62] M. Wang, Structure Effects on Electro-Osmosis in Microporous Media, *J. Heat*  
705 *Transfer* 134(5) (2012) 051020.

706 [63] H. Yoshida, T. Kinjo, H. Washizu, Coupled lattice Boltzmann method for  
707 simulating electrokinetic flows: A localized scheme for the Nernst–Planck model,  
708 *Communications in Nonlinear Science and Numerical Simulation* 19(10) (2014) 3570-  
709 3590.

710 [64] R.A. Patel, J. Perko, D. Jacques, G. De Schutter, K. Van Breugel, G. Ye, A versatile  
711 pore-scale multicomponent reactive transport approach based on lattice Boltzmann

712 method: Application to portlandite dissolution, *Physics and Chemistry of the Earth,*  
713 *Parts A/B/C* 70–71(0) (2014) 127-137.

714 [65] Z. Chai, C. Huang, B. Shi, Z. Guo, A comparative study on the lattice Boltzmann  
715 models for predicting effective diffusivity of porous media, *Int. J. Heat Mass Transfer*  
716 98 (2016) 687-696.

717 [66] H. Yoshida, M. Nagaoka, Multiple-relaxation-time lattice Boltzmann model for the  
718 convection and anisotropic diffusion equation, *Journal of Computational Physics*  
719 229(20) (2010) 7774-7795.

720 [67] J.A. Greathouse, R.T. Cygan, J.T. Fredrich, G.R. Jerauld, Adsorption of Aqueous  
721 Crude Oil Components on the Basal Surfaces of Clay Minerals: Molecular Simulations  
722 Including Salinity and Temperature Effects, *The Journal of Physical Chemistry C*  
723 121(41) (2017) 22773-22786.

724 [68] J. Jiang, P. Wang, D. Hou, The mechanism of cesium ions immobilization in the  
725 nanometer channel of calcium silicate hydrate: a molecular dynamics study, *Phys.*  
726 *Chem. Chem. Phys.* 19(41) (2017) 27974-27986.

727 [69] A.G. Kalinichev, R.J. Kirkpatrick, Molecular Dynamics Modeling of Chloride  
728 Binding to the Surfaces of Calcium Hydroxide, Hydrated Calcium Aluminate, and  
729 Calcium Silicate Phases, *Chem. Mater.* 14(8) (2002) 3539-3549.

730 [70] S. Bhattacharya, K.E. Gubbins, Fast Method for Computing Pore Size  
731 Distributions of Model Materials, *Langmuir* 22(18) (2006) 7726-7731.

732 [71] M.Z. Zhang, G. Ye, K. van Breugel, A numerical-statistical approach to  
733 determining the representative elementary volume (REV) of cement paste for  
734 measuring diffusivity, *2010* 60(300) (2010) 14.

735 [72] N. Ukrainczyk, E.A.B. Koenders, Representative elementary volumes for 3D  
736 modeling of mass transport in cementitious materials, *Modell. Simul. Mater. Sci. Eng.*  
737 22(3) (2014) 035001.

738 [73] M.H.N. Yio, H.S. Wong, N.R. Buenfeld, Representative elementary volume (REV)  
739 of cementitious materials from three-dimensional pore structure analysis, *Cem. Concr.*  
740 *Res.* 102 (2017) 187-202.

741 [74] T. Pan, Y. Liu, Computational Molecular Analysis of Chloride Transport in  
742 Hydrated Cement Paste, *Transportation Research Record: Journal of the Transportation*  
743 *Research Board* 2113 (2009) 31-40.

744 [75] T. Pan, K. Xia, L. Wang, Chloride binding to calcium silicate hydrates (C-S-H) in  
745 cement paste: a molecular dynamics analysis, *International Journal of Pavement*  
746 *Engineering* 11(5) (2010) 367-379.

747 [76] C. Bucur, M. Olteanu, C. Cristache, M. Pavelescu, Radionuclide transport through  
748 cement matrices, *Rev. Chim.* 61(5) (2010) 458-461.

749 [77] T.C. Hansen, Physical structure of hardened cement paste. A classical approach,  
750 *Mater. Struct.* 19(6) (1986) 423-436.

751